Supplementary Information (SI) for Journal of Materials Chemistry A.
This journal is © The Royal Society of Chemistry 2026

Supporting information

1. Methods of catalysts preparation

Materials

$C_{10}H_{14}O_4Pt$ ($Pt(acac)_2$, 97%), $C_{10}H_{14}O_4Ni$ ($Ni(acac)_2$, 97%), $C_{10}H_{14}O_4Co$ ($Co(acac)_2$, 97%), $C_{15}H_{21}O_6Fe$ ($Fe(acac)_3$, 98%), $C_{15}H_{21}O_6Mn$ ($Mn(acac)_3$, 97%), $C_{15}H_{21}O_6Cr$ ($Cr(acac)_3$, 98%), $C_{15}H_{21}O_6Ga$ ($Ga(acac)_3$, 99%) purchased from Shanghai Maclin. MWNTs-COOH was purchased from Beijing Deco Daojin Technology Co., Ltd. Anhydrous ethanol, KOH (>99.95%), and Nafion membrane solution (5% wt) were purchased from Shanghai Aladdion Bio-Chem Technology Co., Ltd.

Synthesis of catalysts

The catalyst PtNiCoFeMnCrGa/CNT was synthesized via pyrolysis. Taking the catalyst $Pt_{40}Ni_9Co_7Fe_{10}Mn_8Cr_{12}Ga_{14}$/CNT as an example. First, 90 mg of pristine CNT were added to a centrifuge tube containing 30 mL of deionized water. The mixture was homogenized using a homogenizer at 20,000 rpm for 5 min, followed by CNT disruption with a cell disruptor to shear the long pristine CNT into segmented CNT. Subsequently, the CNT suspension was vacuum dried at 333 K for 24 h to obtain the CNT carrier for the catalyst. Subsequently, CNT carrier (30 mg), $Pt(acac)_2$ (0.095 mmol), $Ni(acac)_2$ (0.02864 mmol), $Co(acac)_2$ (0.04137 mmol), $Fe(acac)_3$ (0.02875 mmol), $Mn(acac)_2$ (0.02148 mmol),

$Cr(acac)_3$ (0.08911 mmol), and $Ga(acac)_3$ (0.05355 mmol) was weighed into a mortar and thoroughly mixed by grinding. Subsequently, the mixed powder was placed in a tube furnace and heated at a rate of 30 K min^{-1} to 573 K under an H_2/Ar atmosphere, held at this temperature for 2 h, then heated at 30 K min^{-1} to 873 K and held for another 2 h. Finally, the furnace was allowed to cool naturally to room temperature, yielding the final catalyst. For ease of expression, the catalyst PtNiCoFeMnCrGa/CNT will be abbreviated as Gax in the following content, where x denotes the percentage of Ga in the catalyst, with x = 0, 9, 14, 18. For example, $Pt_{40}Ni_{13}Co_{11}Fe_{13}Mn_{11}Cr_{12}$/CNT will be abbreviated as Ga_0, while $Pt_{40}Ni_9Co_7Fe_{10}Mn_8Cr_{12}Ga_{14}$/CNT will be abbreviated as Ga_{14}.

2. Characterization of catalysts

Scanning electron microscopy (SEM) was employed to examine the surface morphology and microstructure of the catalyst after annealing. Transmission electron microscopy (TEM, Titan G2 60-300) was utilized to characterize nanoscale morphology, crystal structure, and elemental distribution information. X-ray diffraction (XRD, Smart Lab 3 kW with Kα radiation) was applied to investigate the phase composition and crystal structure information of the catalyst. X-ray photoelectron spectroscopy (XPS, Thermo Fisher Scientific K-Alpha) was employed to investigate elemental distribution and valence states on the catalyst

surface. XPS data were processed using XPSPEAK software and charge-corrected with a C 1s peak position of 284.6 eV.

3. Electrochemical Testing

3.1 Reference Electrode Calibration

The calibration method for the conversion relationship between Hg/HgO electrode potential and RHE potential refered to the work of Niu et al[1]. In a standard closed three-electrode system, a Pt mesh electrode served as the working electrode, a Pt sheet electrode as the counter electrode, and a Hg/HgO electrode as the reference electrode. Electrolytes consisting of 1 M KOH and 0.1 M KOH were used to calibrate the conversion relationship between the Hg/HgO electrode potential and the RHE potential in 1 M KOH and 0.1 M KOH solutions, respectively. First, H_2 was continuously bubbled into the electrolyte for 30 min to saturate both the electrolyte and the headspace with H_2. Subsequently, cyclic voltammetry (CV) was performed at a scan rate of 5 mV s^{-1} to determine the thermodynamic equilibrium potential for hydrogen evolution in the respective electrolyte. This potential was calculated as the average of the two potential values where the current value was 0, as shown in Figures S14 and S15. The conversion relationship between the Hg/HgO electrode and the RHE potential in 1 M KOH is: E(RHE) = E(Hg/HgO) + 0.9235 V. In 0.1 M KOH, the conversion relationship is: E(RHE) = E(Hg/HgO) +

0.887 V.

3.2 HER and OER Tests

In a standard three-electrode system, 1 M KOH served as the electrolyte, a 3 mm diameter glassy carbon electrode (GCE) functioned as the working electrode, a Hg/HgO electrode acted as the counter electrode, and a Pt sheet electrode served as the reference electrode for HER and OER measurements. The catalyst ink preparation method referred to the work of Wang et al[2]. 5 mg of catalyst was added to 900 μL of ethanol and 100 μL of Nafion (5 wt.%) solution, then sonicated for 30 min to ensure thorough mixing. Subsequently, 4 μL of the ink (containing 20 μg of catalyst) was uniformly drop-coated onto the surface of a GCE to serve as the working electrode for both HER and OER. For the HER test, H_2 was continuously introduced into 1 M KOH to saturate the electrolyte and the space above it with H_2. Subsequently, the working electrode was activated using CV at a scan rate of 10 mV s^{-1} for 20 cycles over the potential range of 0 to -0.01 V vs. RHE. The HER polarization curve of the catalyst was tested using linear sweep voltammetry (LSV) at a scan rate of 5 mV s^{-1} over the potential range of 0 to -0.4 V. Additionally, to test the polarization curve of catalyst Ga_{14} under industrial current density conditions, LSV testing was conducted at a scan rate of 5 mV s^{-1} over the potential range of 0 to -0.15 V. Working electrodes were prepared using carbon paper as the substrate with identical catalyst loading rates. The

HER stability of the catalysts was evaluated via chronopotentiometry (CP) at a current density of 10 mA cm^{-2}. The results (E) were normalized relative to the initial potential (E_0) as (E/E_0). For OER testing, O_2 was continuously introduced into 1 M KOH solution to saturate both the electrolyte and the space above it with O_2. The CV activation range is 1.25 V - 1.55 V, and the LSV test range is 1.2 V - 1.6 V. The LSV test range at industrial current density was 1.2 V - 1.65 V. Other test details were consistent with HER and are therefore omitted. For the electrochemical active surface area (ECSA) of catalyst Ga_x, the open-circuit potential was first measured. Subsequently, cyclic voltammetry (CV) tests were conducted at different scan rates within a potential range centered at the open-circuit potential and spanning 0.1 V. The scan rates were 20 mV s^{-1}, 40 mV s^{-1}, 60 mV s^{-1}, 80 mV s^{-1}, 100 mV s^{-1}, and 120 mV s^{-1}. The current density at the open-circuit potential was selected to obtain C_{dl} for characterizing the ECSA. For the electrochemical impedance spectroscopy (EIS) of catalyst Ga_x, the open circuit voltage of the catalyst was first measured. Subsequently, the electrochemical impedance of the catalyst was recorded from 100 kHz to 0.1 Hz at the open-circuit voltage.

3.4 ORR and OER Tests

In a standard three-electrode system, 0.1 M KOH served as the electrolyte. Using a Hg/HgO electrode as the reference electrode, a graphite electrode

as the counter electrode, and a rotating disk electrode (RDE) with a glassy carbon disk diameter of 3 mm as the working electrode, tests for the oxygen reduction reaction (ORR) and oxygen evolution reaction (OER) were conducted. The preparation method of the catalyst ink referred to the work of Wang et al[2]. Spin-coated the catalyst onto the RDE glassy carbon disc at a rotation speed of 600 rpm to achieve a loading of 20 μg_{Pt} cm^{-2}. For the ORR test, N_2 was first continuously purged into 0.1 M KOH for 30 min to saturate both the electrolyte and the space above it with N_2. Subsequently, CV activation was performed at a scan rate of 5 mV s^{-1} over the potential range of 0.2 V to 1.05 V, with 20 cycles completed. Following this, LSV testing was conducted at a scan rate of 1 mV s^{-1} over the potential range of 0.2 V to 1.2 V at a rotation speed of r = 1600 rpm, maintaining continuous N_2 flow throughout the testing process. Subsequently, O_2 was continuously introduced into 0.1 M KOH for 30 min to saturate the electrolyte and the space above it with O_2. Cyclic voltammetry (CV) was then performed at a scan rate of 5 mV s^{-1} over the potential range of 0.2 V to 1.2 V. Subsequently, linear sweep voltammetry (LSV) was conducted at a scan rate of 1 mV s^{-1} over the same potential range at a rotation speed of r = 1600 rpm, with continuous O_2 supply maintained throughout the testing process. Finally, the LSV curve obtained under O_2 flow was subtracted from the LSV curve measured under N_2 flow to yield the ORR polarization curve of the

catalyst. The ORR stability of the catalysts was evaluated using the chronoamperometric method (i-t) at their respective half-wave potentials. The results (i) were normalized relative to the initial potential (i_0) as (i/i_0). For the OER test, O_2 was first continuously bubbled into 0.1 M KOH solution to saturate both the electrolyte and the space above it with O_2, followed by 20 cycles of CV activation at a scan rate of 10 mV s^{-1} within the potential range of 1.25 V to 1.5 V. Finally, LSV testing was conducted at a rotation speed of 1600 rpm with a scan rate of 5 mV s^{-1} across the potential range of 1.2 V to 1.6 V.

3.5 Overall Water Splitting Tests

The overall water splitting performance of the catalyst was evaluated using an anion exchange membrane (AEM) electrolytic cell and a DC power supply R-SPS3020-USB. 1 M KOH was used as the electrolyte for complete water splitting, with NiFe mesh serving as the catalyst support. 10 mg of catalyst were mixed with 800 μL ethanol and 40 μL Nafion (5 wt.%) solution. The mixture was stolen for 30 min to ensure thorough dispersion. The solution was then uniformly sprayed onto a 1 cm × 1 cm NiFe mesh to form one electrode for the overall water splitting reaction. This electrode was subsequently air-dried at 333 K for 1 hour. The other electrode for the overall water splitting reaction was prepared using the same method. To compare with commercial catalysts, 10 mg of Pt/C (20 wt.%) was mixed with 800 μL of ethanol and 40 μL of Nafion (5 wt.%),

while 10 mg of RuO_2 was mixed with 600 μL of ethanol and 30 μL of Nafion (5 wt.%). Electrodes loaded with commercial catalysts were prepared using the same method. The anion exchange membranes were immersed in 1 M KOH at 333 K for 15 min and finally assembled into complete AEM for testing. To minimize the impact of electrolyte changes during the reaction process, the electrolyte was circulated through the AEM via a circulation pump. After heating the electrolyte and AEM to 333 K, the polarization curve for water electrolysis was first tested within a voltage range of 1.2 V to 3.75 V at a scan rate of 5 mV s^{-1}. Finally, the stability of complete water splitting was evaluated using chronopotentiometry at a current density of 1 A cm^{-2}.

3.6 Assembly and Testing of Aqueous Rechargeable Zinc-Air Batteries (RZAB)

Assembly and Testing Methods for Aqueous Rechargeable Zinc-Air Batteries: Reference to Previous Work[3]. Using the recirculating OMS-TR1 mold from Changsha Spring to assemble a battery with a reaction area of 1 cm^2, the flow rate of the recirculation pump was 6 mL min^{-1}. The YLS30T carbon paper-supported catalyst from Suzhou Sinero was assembled with a Ni mesh to form the air cathode. A 0.2 mm thick Zn sheet served as the anode, which was thoroughly polished prior to assembly and sonicated in ethanol for 10 min. The catalyst ink was prepared by mixing 3 mg of catalyst into 400 μL of ethanol and 20 μL of

Nafion (5 wt.%) solution, then sonicated for 30 min to ensure thorough mixing. Compared with commercial catalysts, Pt/C (20 wt.%) and RuO_2 were mixed in a 1:1 mass ratio to prepare the catalyst ink using the same formulation. The catalyst loading on carbon paper was 1 mg cm^{-2}. A mixed solution of 6 M KOH and 0.2 M $Zn(CH_3COO)_2$ served as the battery electrolyte. The open circuit voltage test duration was 20,000 s. The discharging and charging polarization curves undergone linear sweep voltammetry (LSV) testing at a scan rate of 5 mV s^{-1} within the voltage ranges of 1.45 V to 0.2 V and 1.45 V to 3 V, respectively. Long-term discharging tests were conducted at a current density of 10 mA cm^{-2}, while charging/discharging cycle stability tests were performed at 5 mA cm^{-2}. Each cycle comprised both charging and discharging phases lasting 900 s.

3.7 Assembly and Testing of Flexible Rechargeable Zinc-Air Batteries (FRZAB)

A 0.15 mm thick Zn electrode with conductive tabs was used as the cathode, while a 0.3 mm thick carbon paper electrode with conductive tabs served as the catalyst support. Catalyst ink was prepared by mixing 3 mg of catalyst and 3 mg of conductive carbon black into 800 μL of ethanol and 40 μL of Nafion (5 wt.%), followed by ultrasonication for 30 min to ensure thorough mixing. For comparison with a commercial catalyst, a catalyst ink was prepared using the same formulation by

mixing Pt/C (20 wt.%) and RuO_2 in a 1:1 mass ratio. The catalyst loading on the carbon paper electrode was 1 mg cm^{-2}. Polyacrylic acid (PAA) with a thickness of 0.2 mm was soaked in a mixed solution of 6 M KOH and 0.2 M $Zn(CH_3COO)_2$ for 24 h to serve as the gel electrolyte for the battery. The open circuit voltage of the battery was measured using a 2 cm × 4 cm electrode area for 400 s. Long-term discharging tests and charging-discharging cycling stability tests were conducted at a current density of 2 mA cm^{-2}. Each cycle in the stability test involved a 600 s discharging followed by a 600 s charging. Charging-discharging polarization curves were measured using a 1 cm × 1 cm electrode area.

4. Calculation of ORR response

The ORR kinetic current is obtained from the Koutecky-Levich (K-L) equation[3]:

$$\frac{1}{J}=\frac{1}{J_L}+\frac{1}{J_K}=\frac{1}{B\omega^{\frac{1}{2}}}+\frac{1}{J_K} \quad (1)$$

In the equation, J represents the current density, J_L denotes the diffusion-limited current density, JK signifies the kinetic current density, ω indicates the rotational speed (rpm), and B can be calculated using the following formula:

$$B=0.2n_0F(D_0)^{\frac{2}{3}}v^{-\frac{1}{6}} \quad (2)$$

In the equation, n represents the number of electrons transferred, F denotes Faraday constant (96485 C mol^{-1}), C_0 is the volume concentration of O_2 in 0.1 M KOH (1.2×10^{-6} mol cm^{-3}), D_0 is the diffusion coefficient of O_2 in 0.1 M KOH, and υ is the kinetic viscosity of the 0.1 M KOH solution.

5. DFT calculation

In this work, calculations of reaction free energies and projected density of states (PDOS) for the hydrogen evolution reaction (HER) and oxygen evolution reaction (OER) processes in the catalyst system were performed using the Vienna Atypical System Performance (VASP) ab initio simulation software package. The computational model was constructed based on a comprehensive analysis of transmission electron microscopy (TEM) and X-ray diffraction (XRD) results. The exchange-correlation interaction was modeled using the Perdew-Burke-Ernzerhof (PBE) functional within the generalized gradient approximation (GGA) framework. Electron-ion interactions were described via the projected augmented plane wave (PAW) method. Through convergence testing, a plane-wave cutoff energy of 500 eV was selected. A self-consistent convergence criterion of 10^{-5} eV was set for electron energies. Geometric optimization was completed when the change in atomic force was less than 0.05 eV. A 15 Å vacuum layer was applied along the Z-direction to mitigate self-interactions caused by periodic mirroring. Both geometric

relaxation and electronic relaxation Brillouin zone integration employed a 5 × 5 × 1 k-point grid[4]. The reaction free energy correction was calculated using the following equation: $\Delta G = \Delta E + \Delta ZPE + \Delta H - T\Delta S$ where: ΔE represents the reaction energy calculated by DFT; ΔZPE is the zero-point energy correction; ΔH is the enthalpy change (cumulative heat capacity) from 0 K to 298.15 K; and ΔS denotes the entropy change.

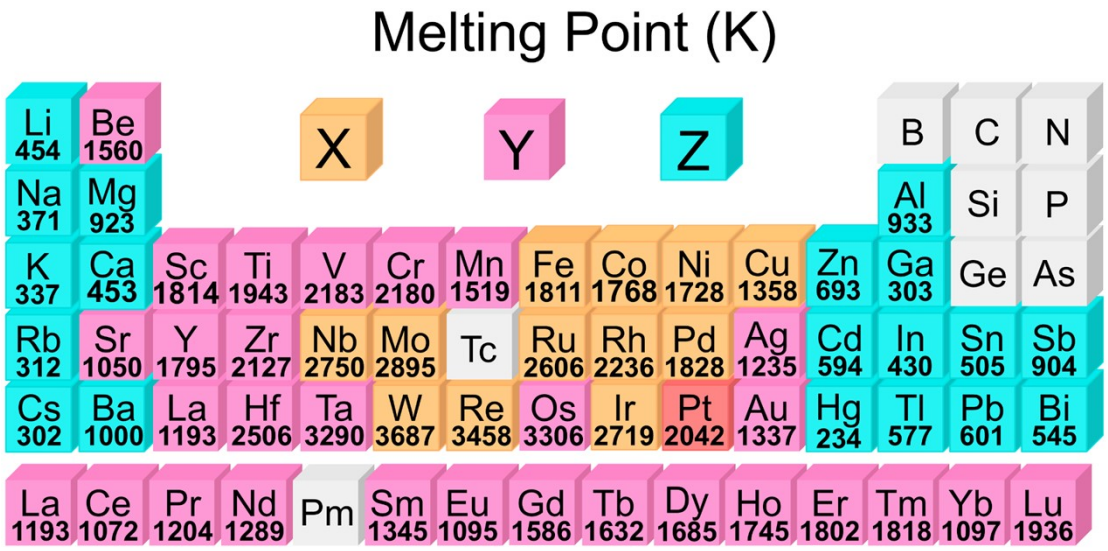

Figure S1. Melting Point of metal elements.

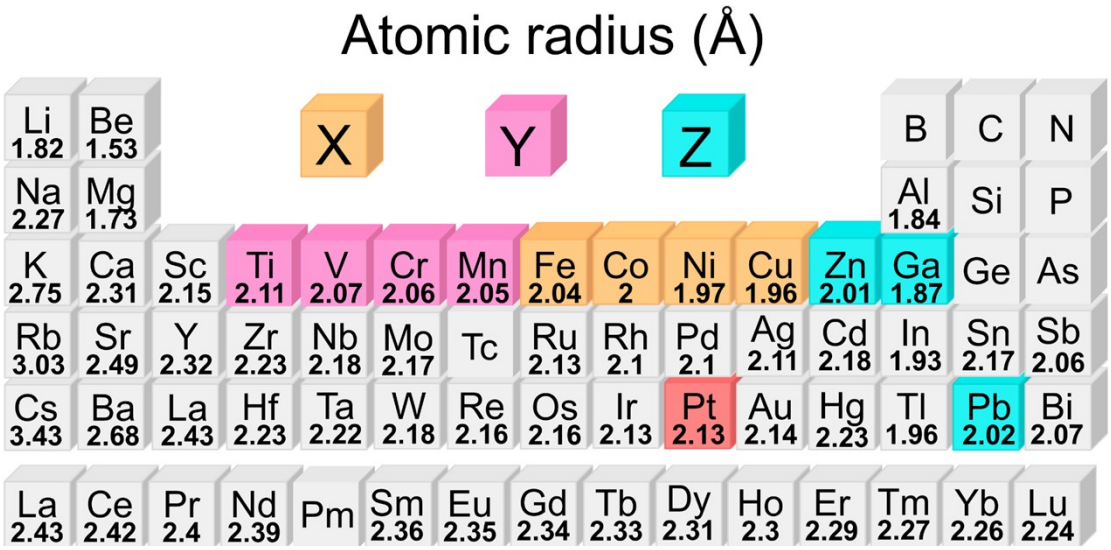

Figure S2. Atomic radius of metal elements.

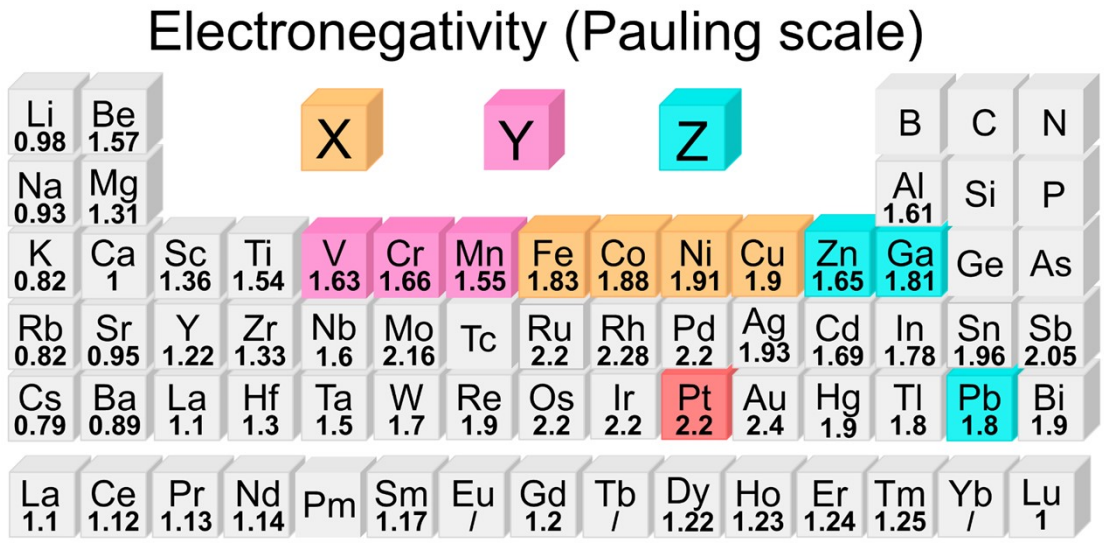

Figure S3. Electronegativity (Pauling scale) of metal elements.

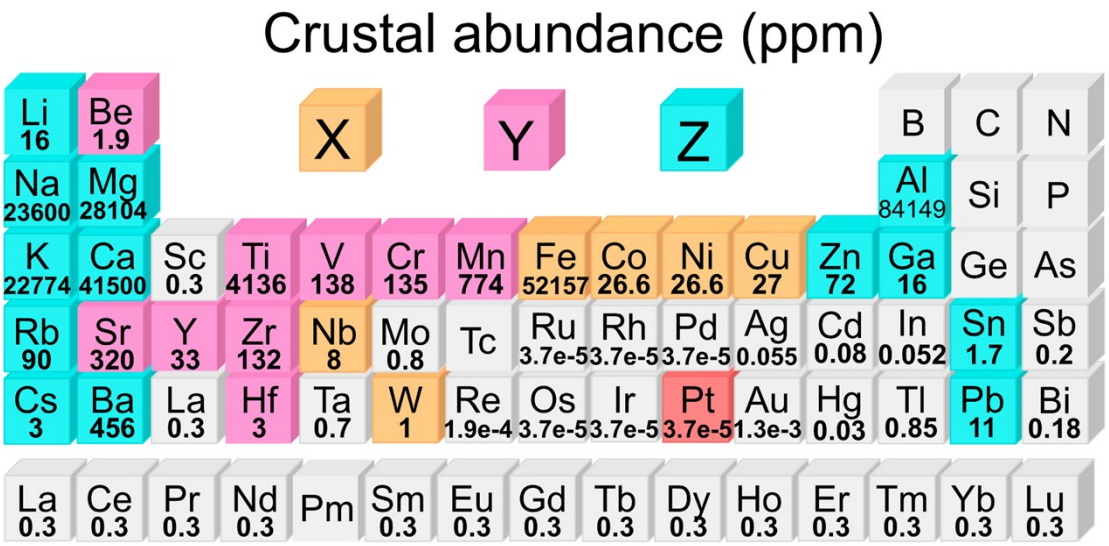

Figure S4. Crustal abundance of metal elements.

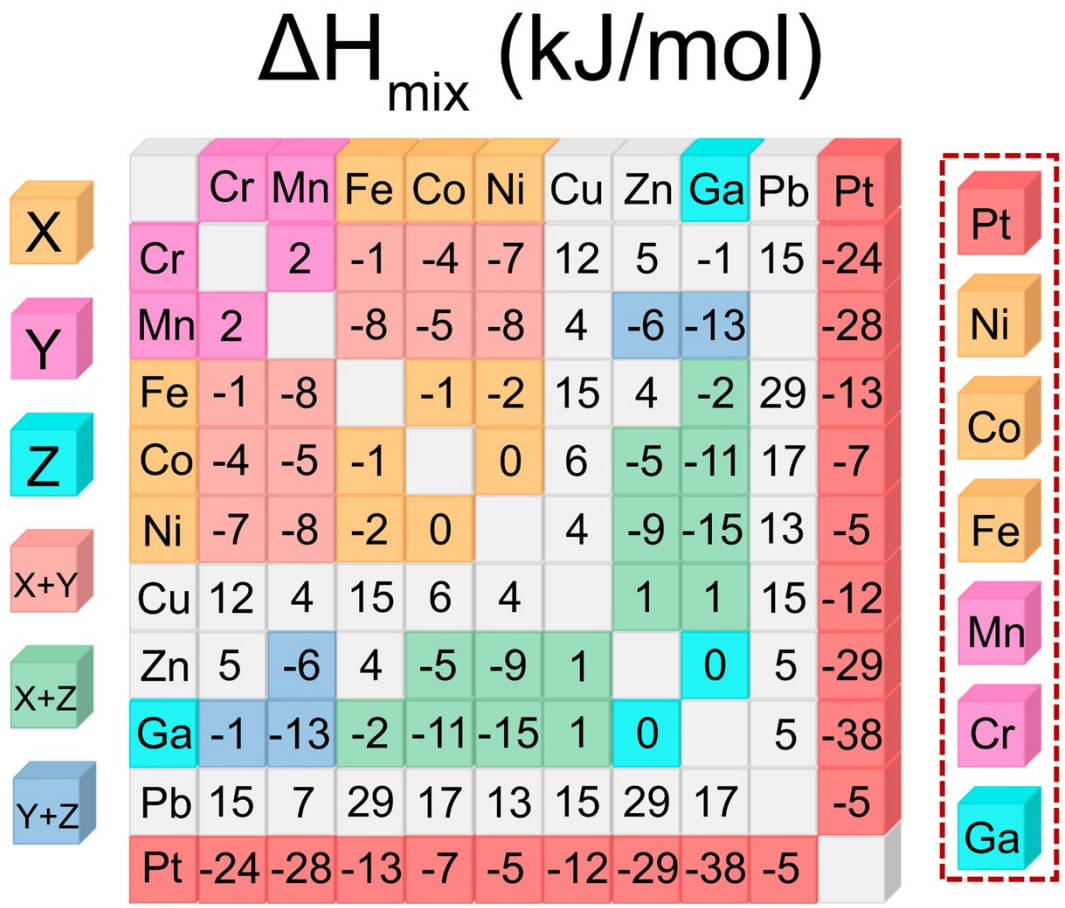

Figure S5. Mixed enthalpy of some metal elements.

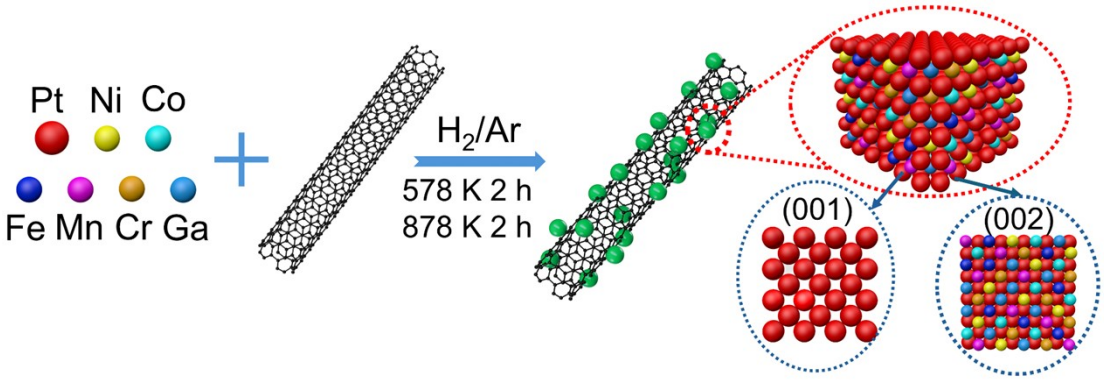

Figure S6. Flowchart of PtNiCoFeMnCrGa/CNT preparation process.

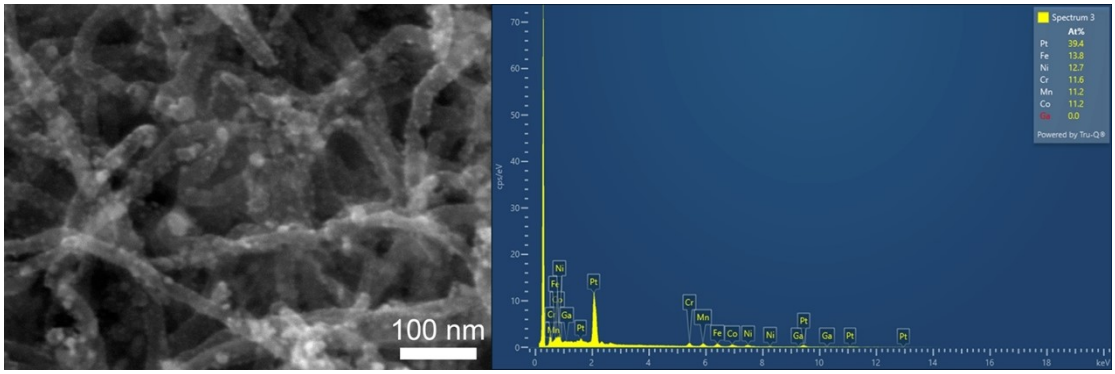

Figure S7. SEM and EDS image of $Pt_{40}Ni_{13}Co_{11}Fe_{13}Mn_{11}Cr_{12}$/CNT.

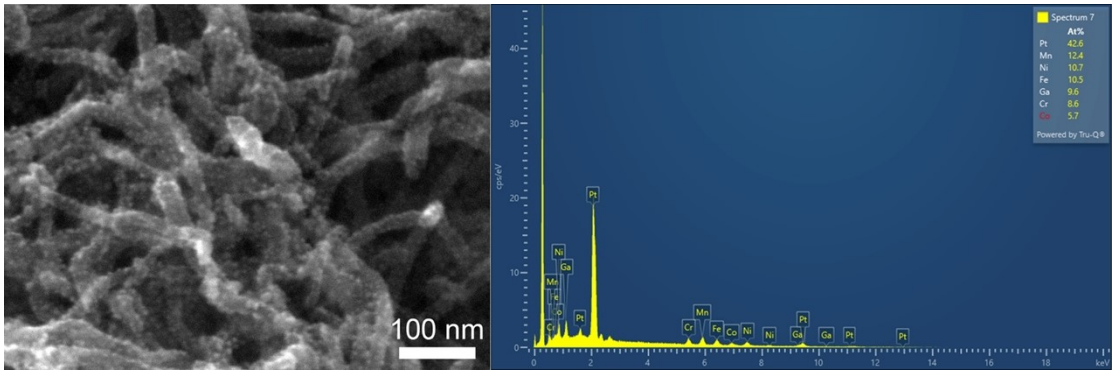

Figure S8. SEM and EDS image of $Pt_{42}Ni_{11}Co_6Fe_{11}Mn_{12}Cr_9Ga_9$/CNT.

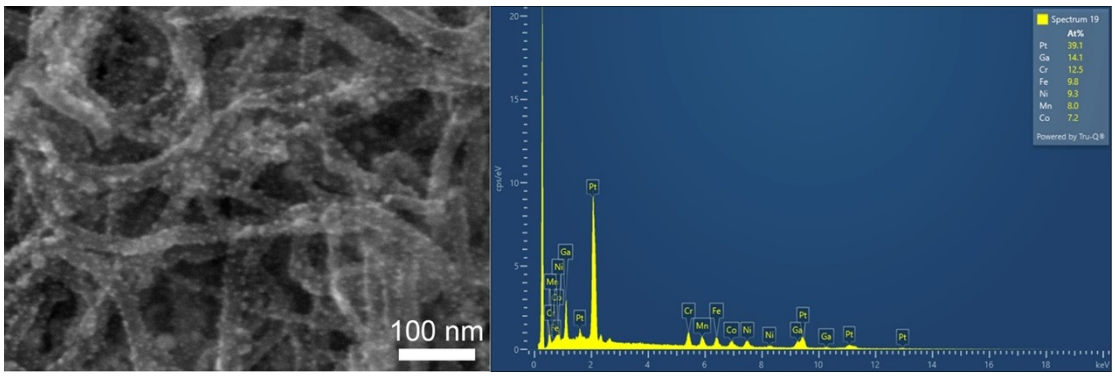

Figure S9. SEM and EDS image of $Pt_{40}Ni_9Co_7Fe_{10}Mn_8Cr_{12}Ga_{14}$/CNT.

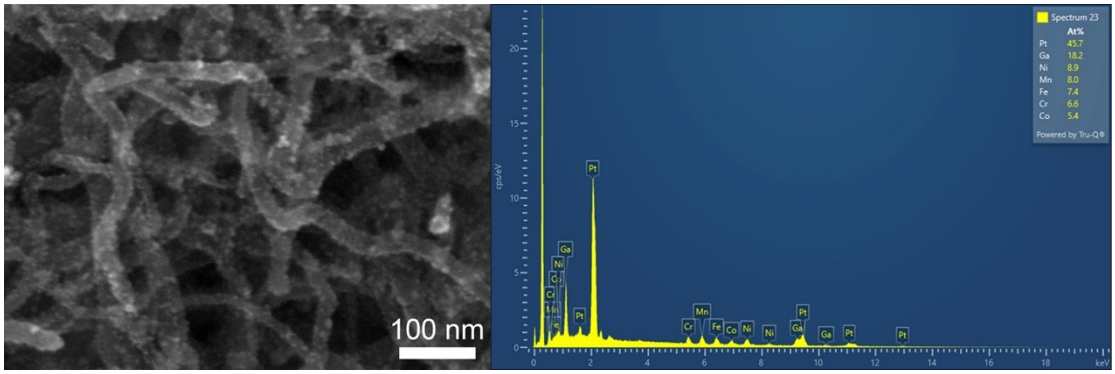

Figure S10. SEM and EDS image of $Pt_{45}Ni_9Co_6Fe_7Mn_8Cr_7Ga_{18}$/CNT.

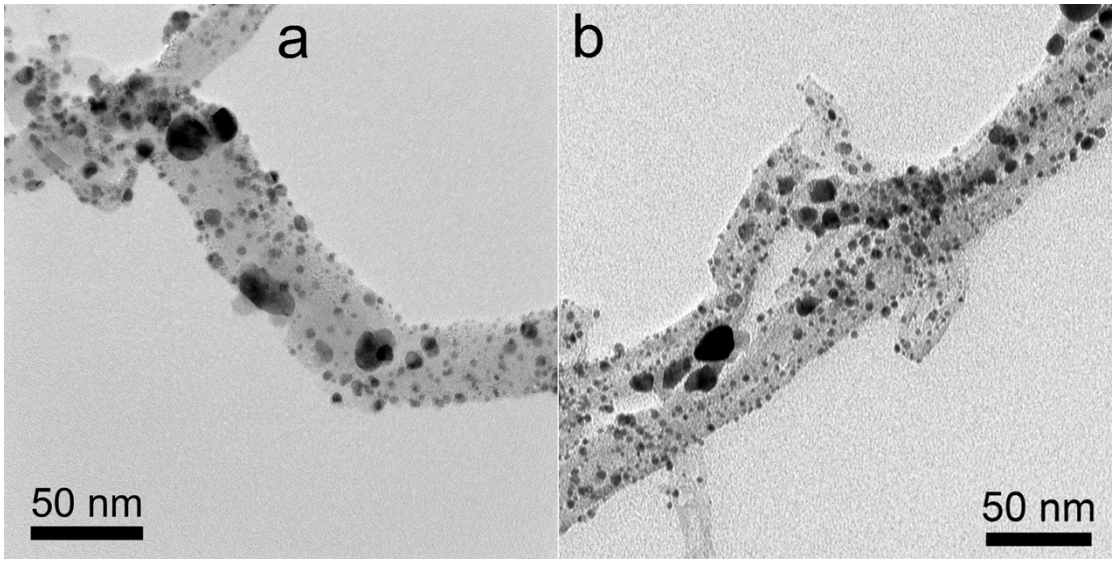

Figure S11. TEM morphology of $Pt_{40}Ni_{13}Co_{11}Fe_{13}Mn_{11}Cr_{12}$/CNT.

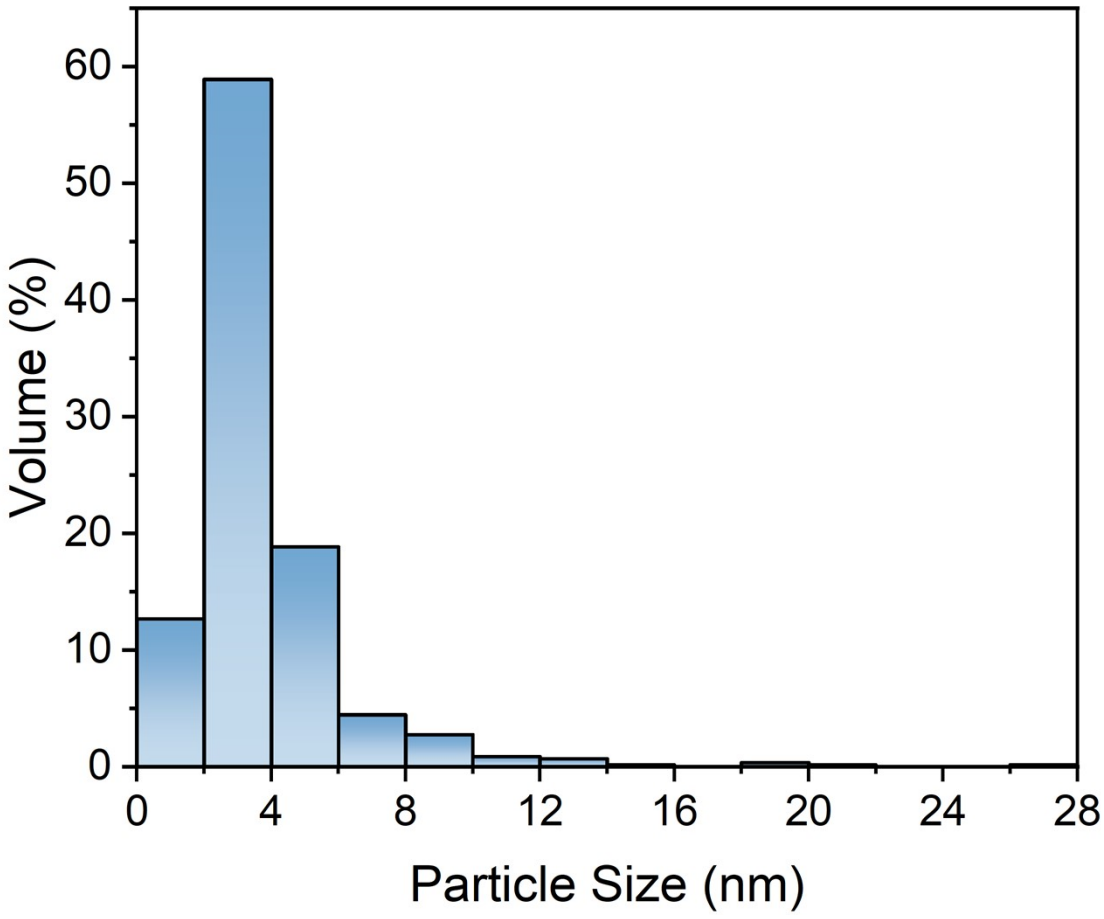

Figure S12. Particle size distribution of $Pt_{40}Ni_{13}Co_{11}Fe_{13}Mn_{11}Cr_{12}$/CNT.

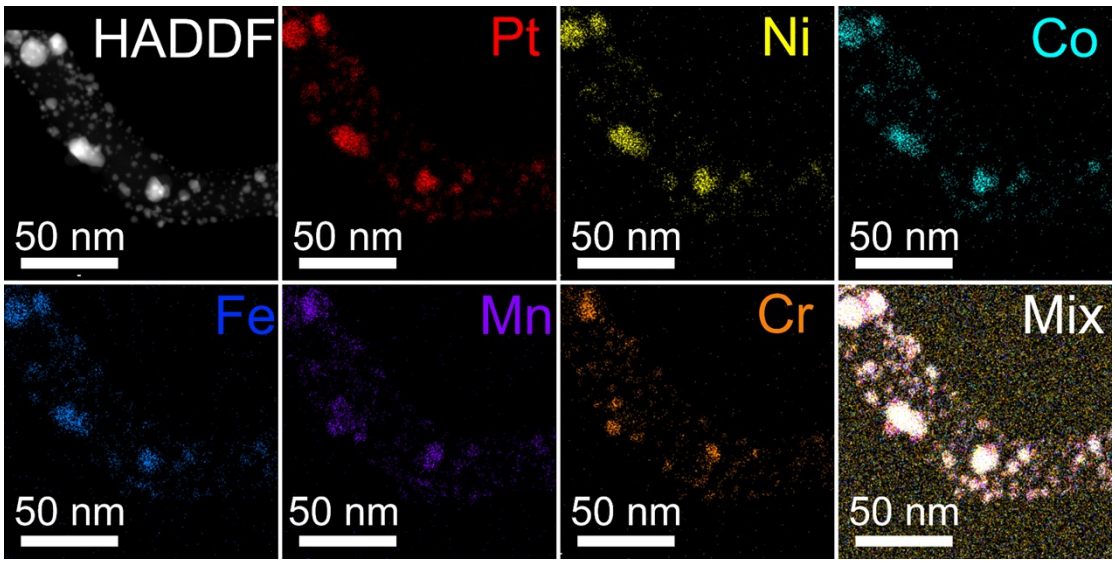

Figure S13. HADDF and EDS mapping of

$Pt_{40}Ni_{13}Co_{11}Fe_{13}Mn_{11}Cr_{12}$/CNT.

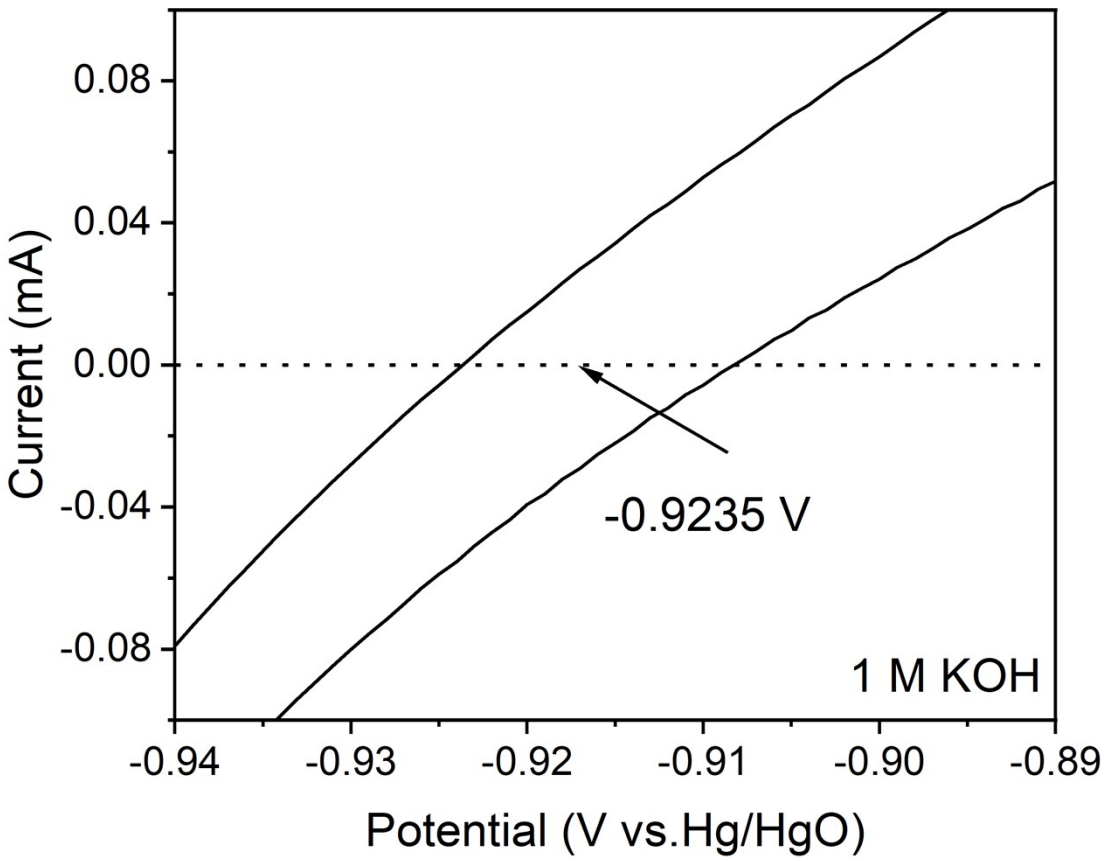

Figure S14. CV curve of Hg/HgO electrode calibration in 1 M KOH.

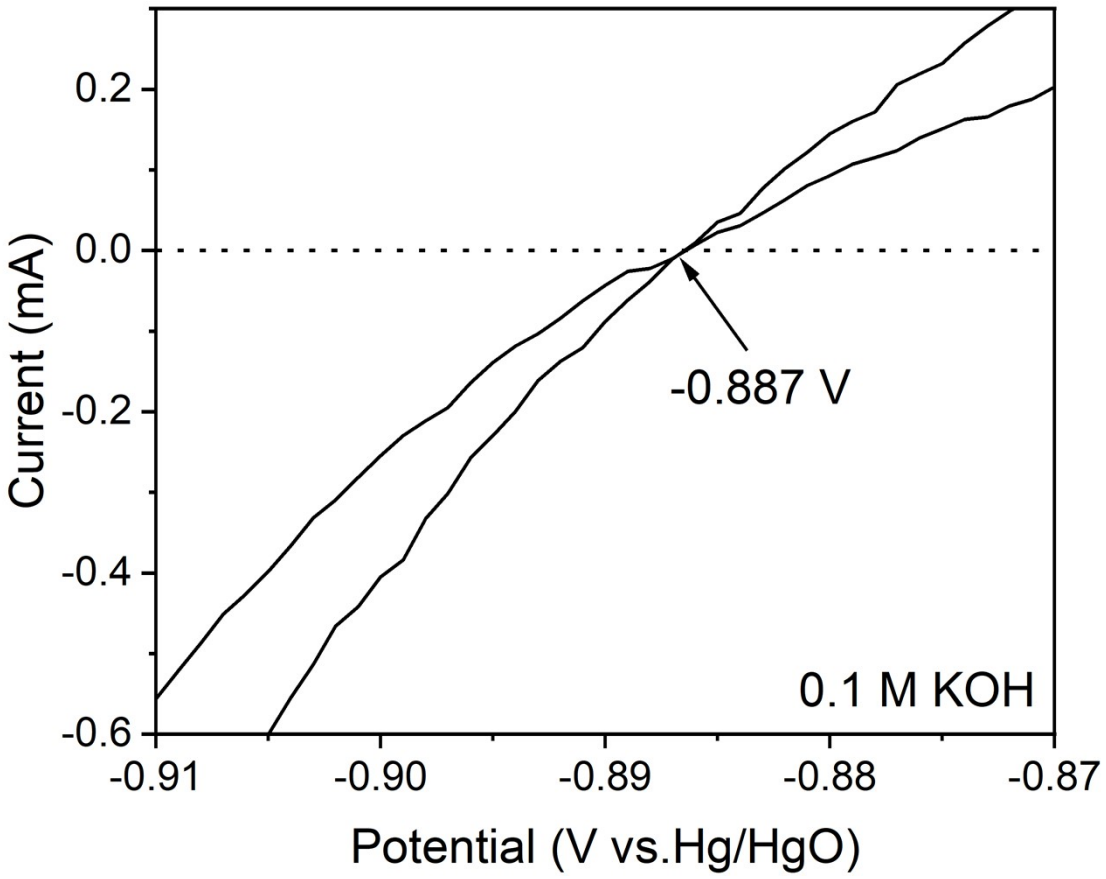

Figure S15. CV curve of Hg/HgO electrode calibration in 0.1 M KOH.

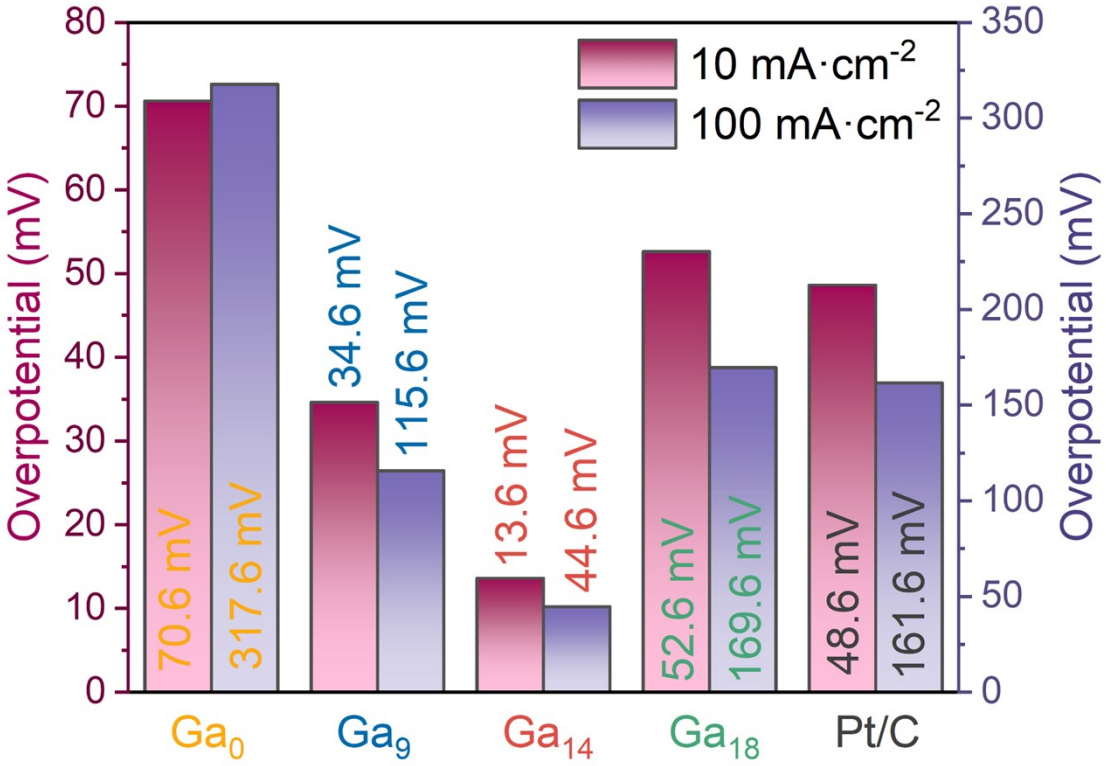

Figure S16. Bar chart of HER overpotential at 10 mA cm^{-2} and 100 mA cm^{-2} in 1 M KOH of PtNiCoFeMnCrGa/CNT and Pt/C.

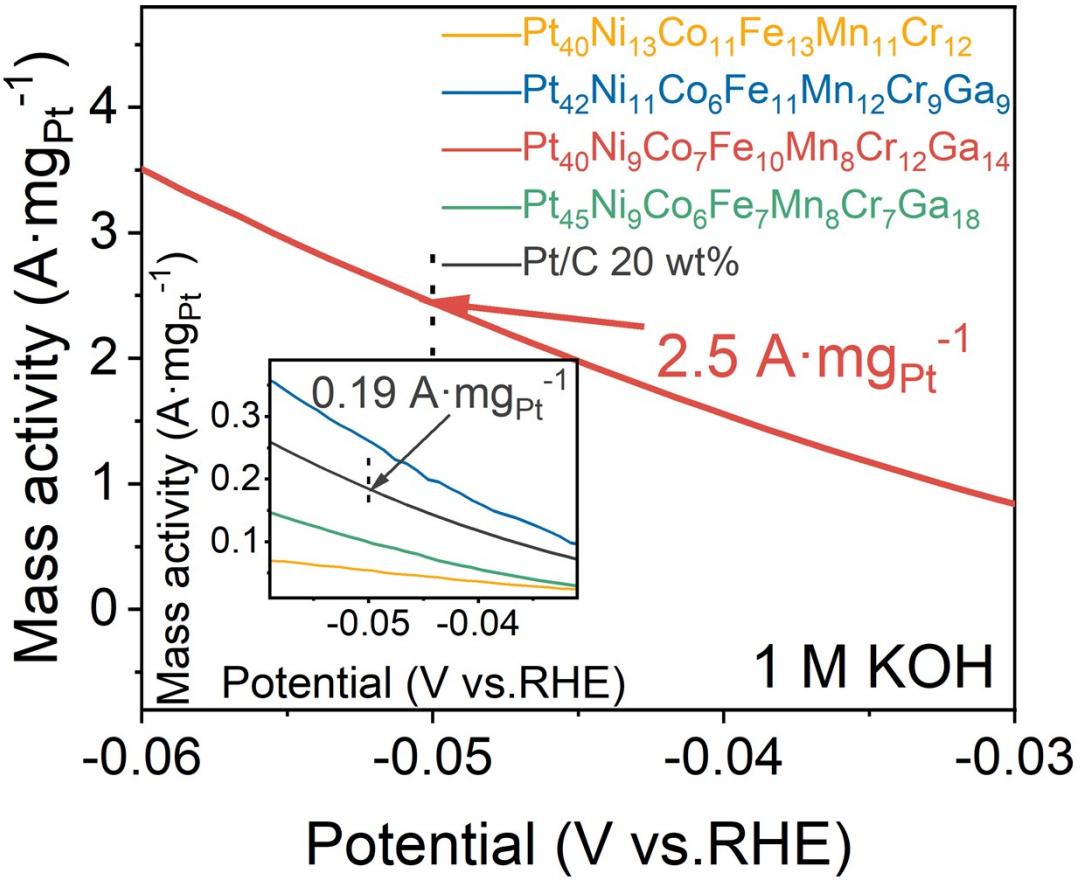

Figure S17. Mass activity of HER of PtNiCoFeMnCrGa/CNT and Pt/C.

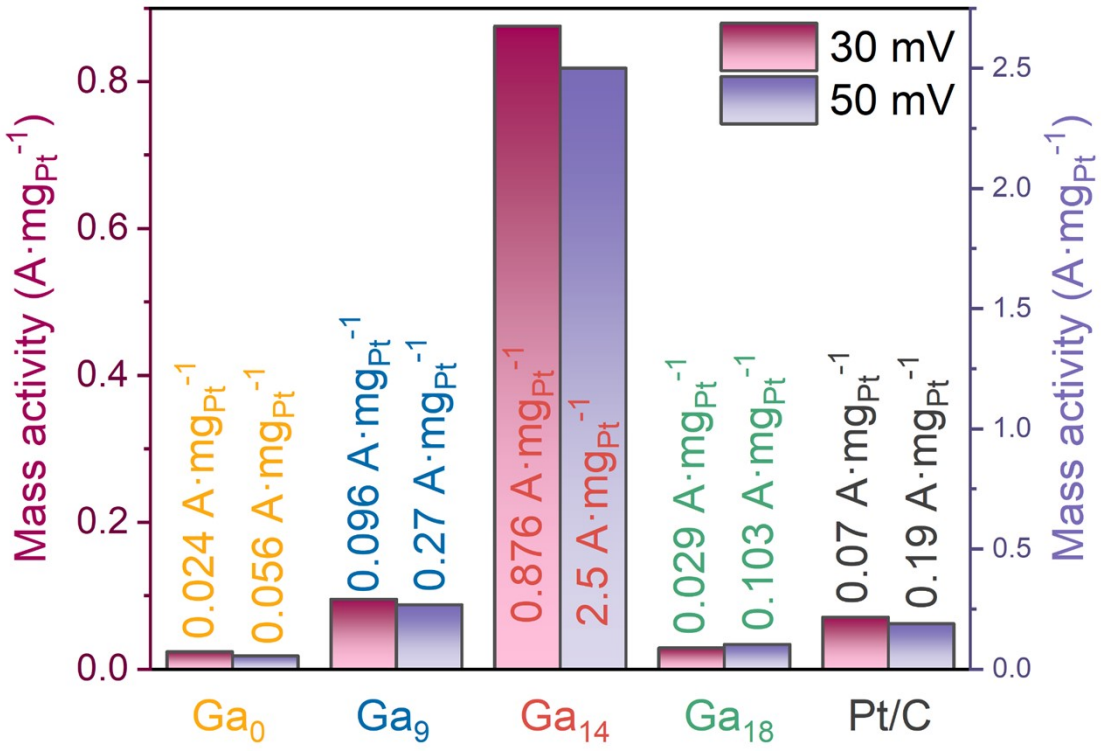

Figure S18. Bar chart of HER mass activity at an overpotential of 20 mV and 50 mV in 1 M KOH of PtNiCoFeMnCrGa/CNT and Pt/C.

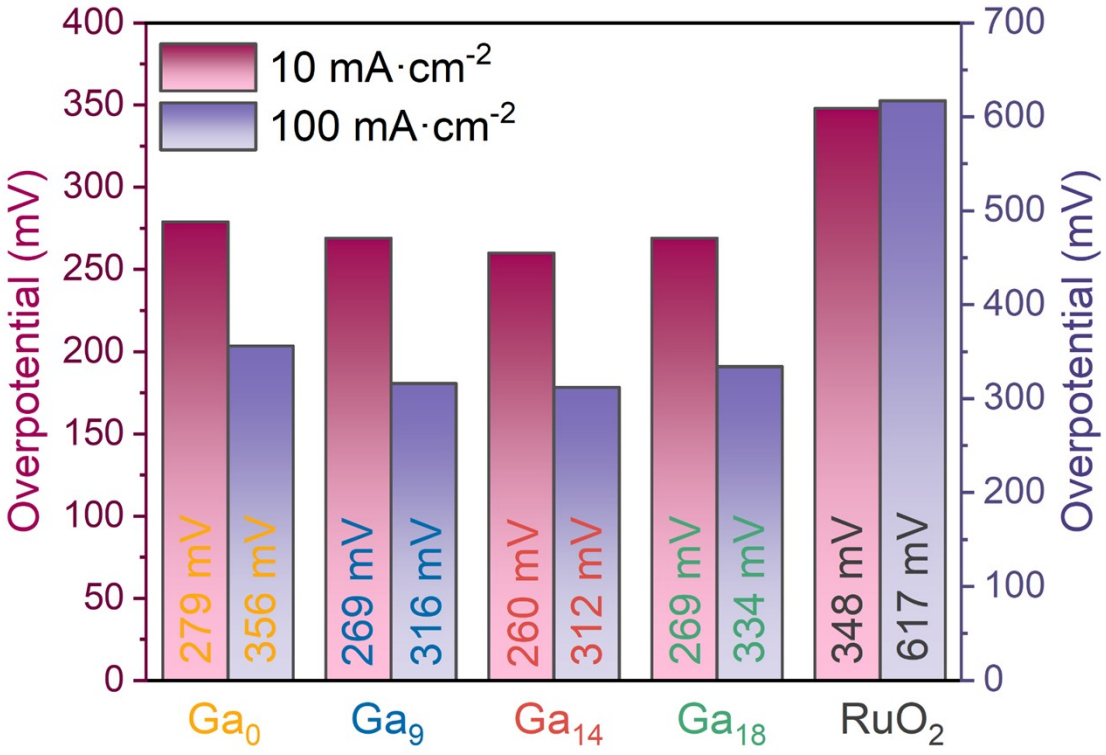

Figure S19. Bar chart of OER overpotential at 10 mA cm^{-2} and 100 mA cm^{-2} in 1 M KOH of PtNiCoFeMnCrGa/CNT and RuO_2.

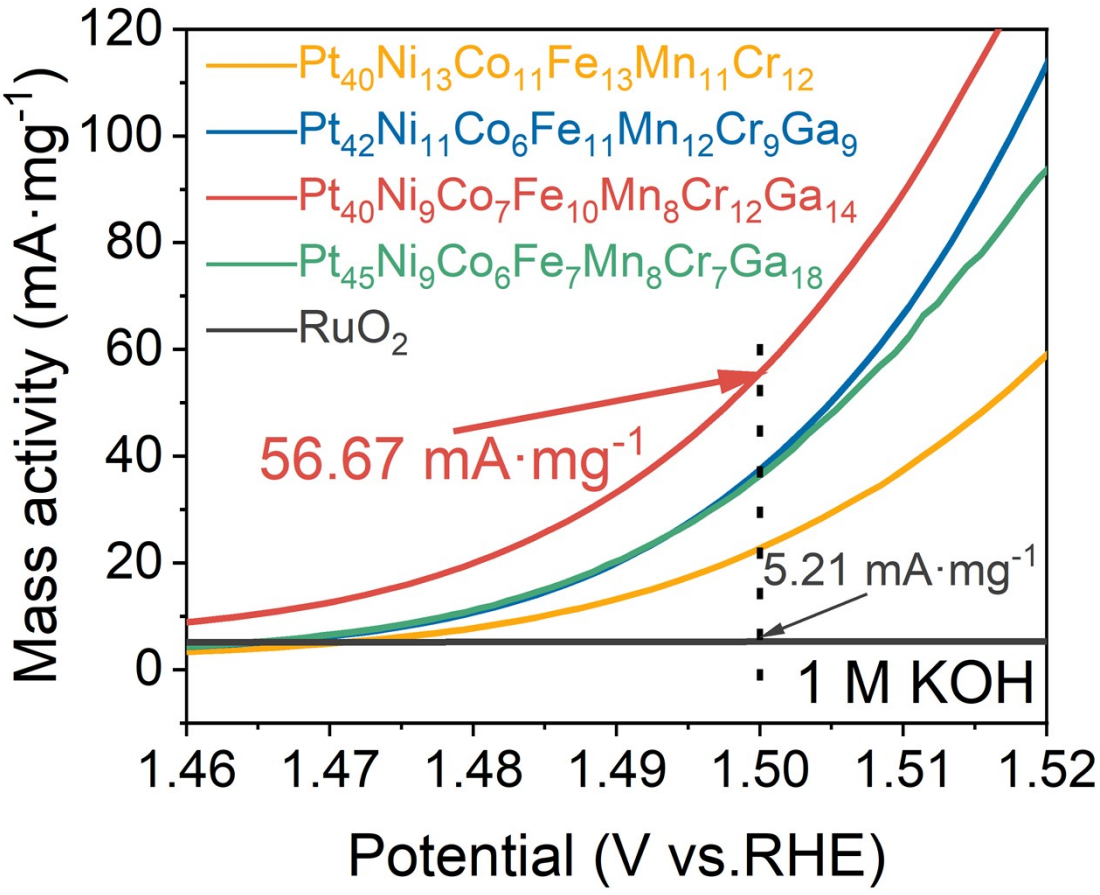

Figure S20. Mass activity of OER of PtNiCoFeMnCrGa/CNT and RuO_2.

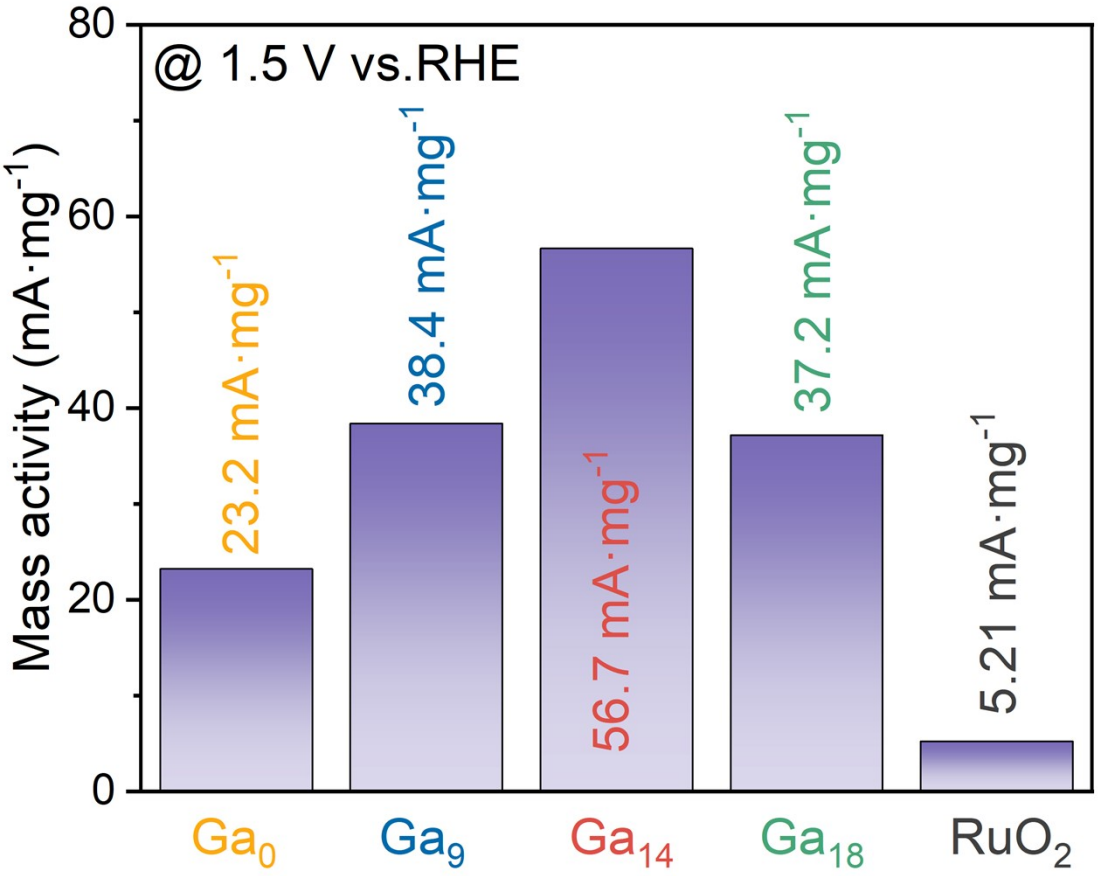

Figure S21. Bar chart of OER mass activity at a potential of 1.5 V vs.RHE in 1 M KOH of PtNiCoFeMnCrGa/CNT and RuO_2.

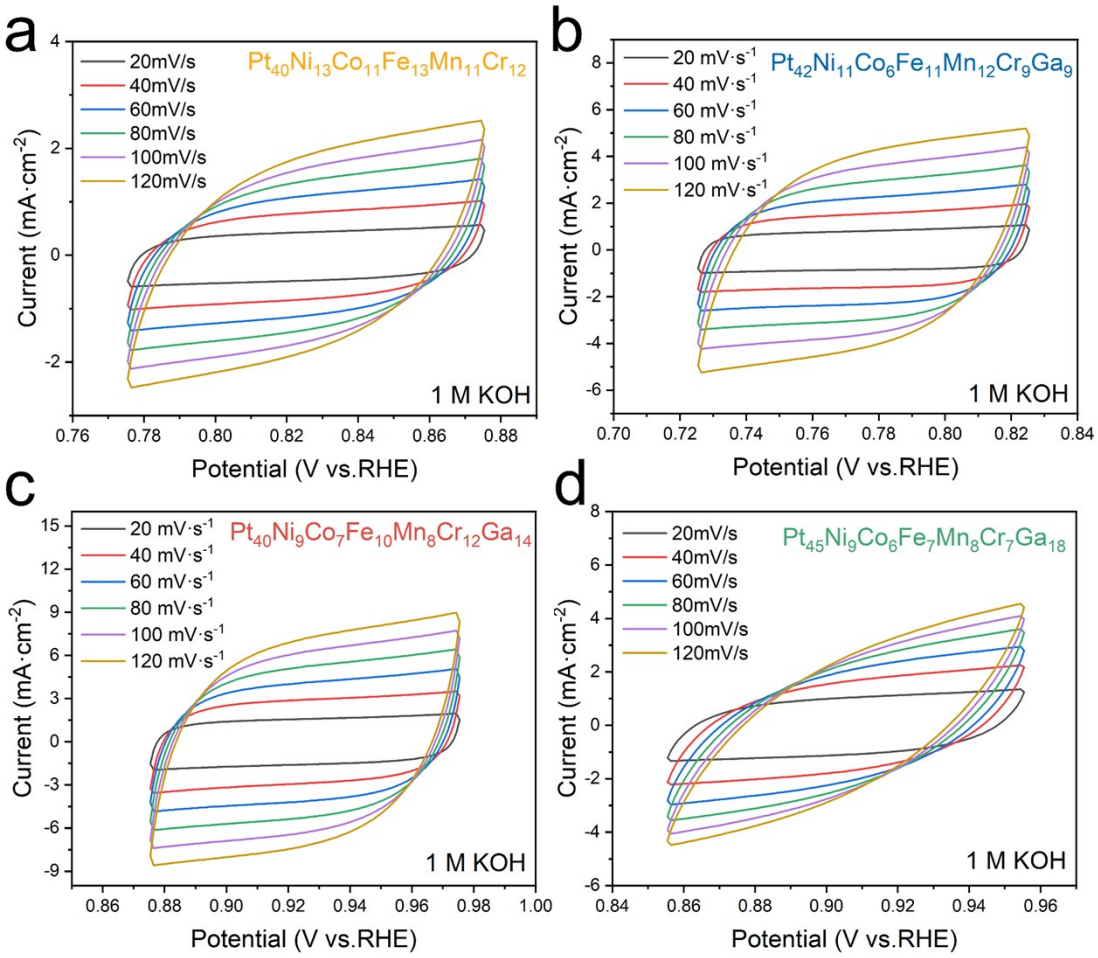

Figure S22. CV curves for ECSA in 1 M KOH of (a) $Pt_{40}Ni_{13}Co_{11}Fe_{13}Mn_{11}Cr_{12}$/CNT; (b) $Pt_{42}Ni_{11}Co_6Fe_{11}Mn_{12}Cr_9Ga_9$/CNT; (c) $Pt_{40}Ni_9Co_7Fe_{10}Mn_8Cr_{12}Ga_{14}$/CNT; (d) $Pt_{45}Ni_9Co_6Fe_7Mn_8Cr_7Ga_{18}$/CNT.

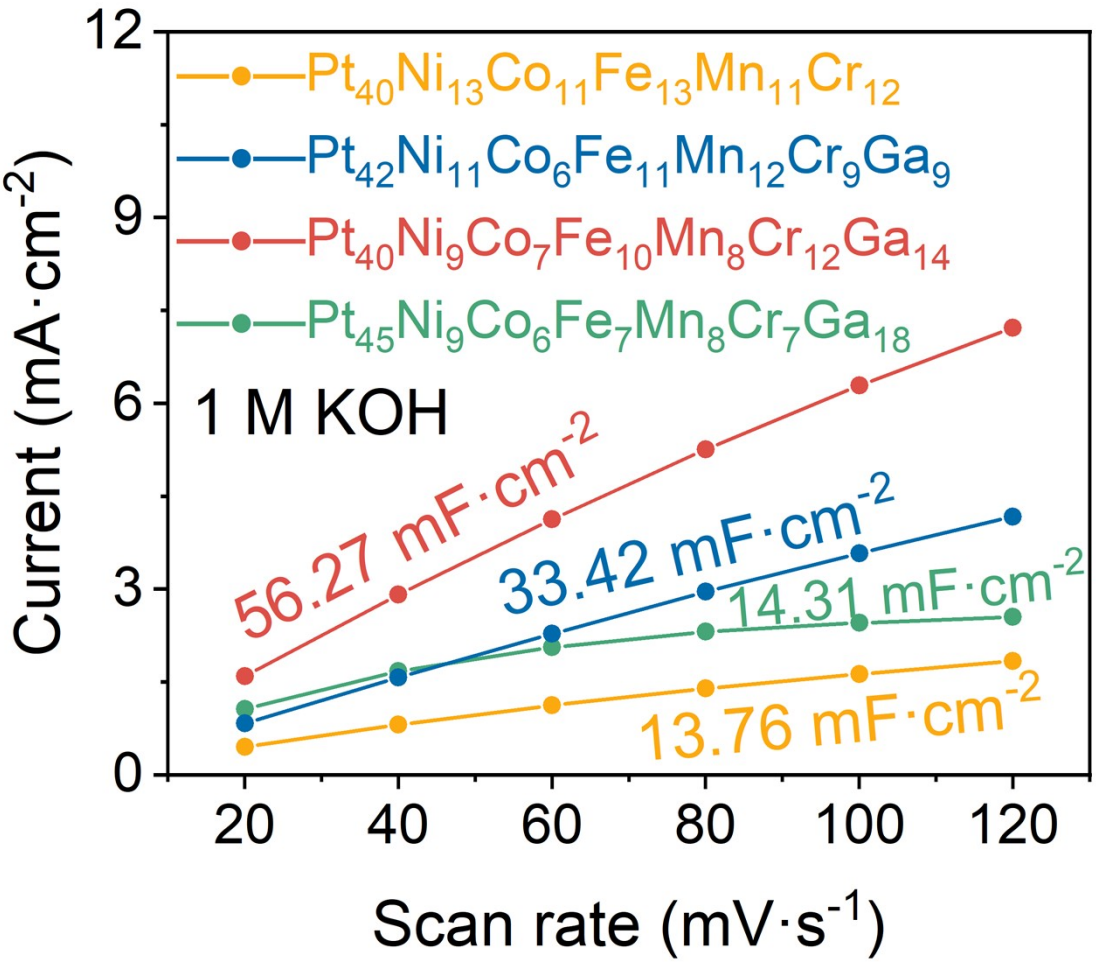

Figure S23 ECSA of PtNiCoFeMnCrGa/CNT.

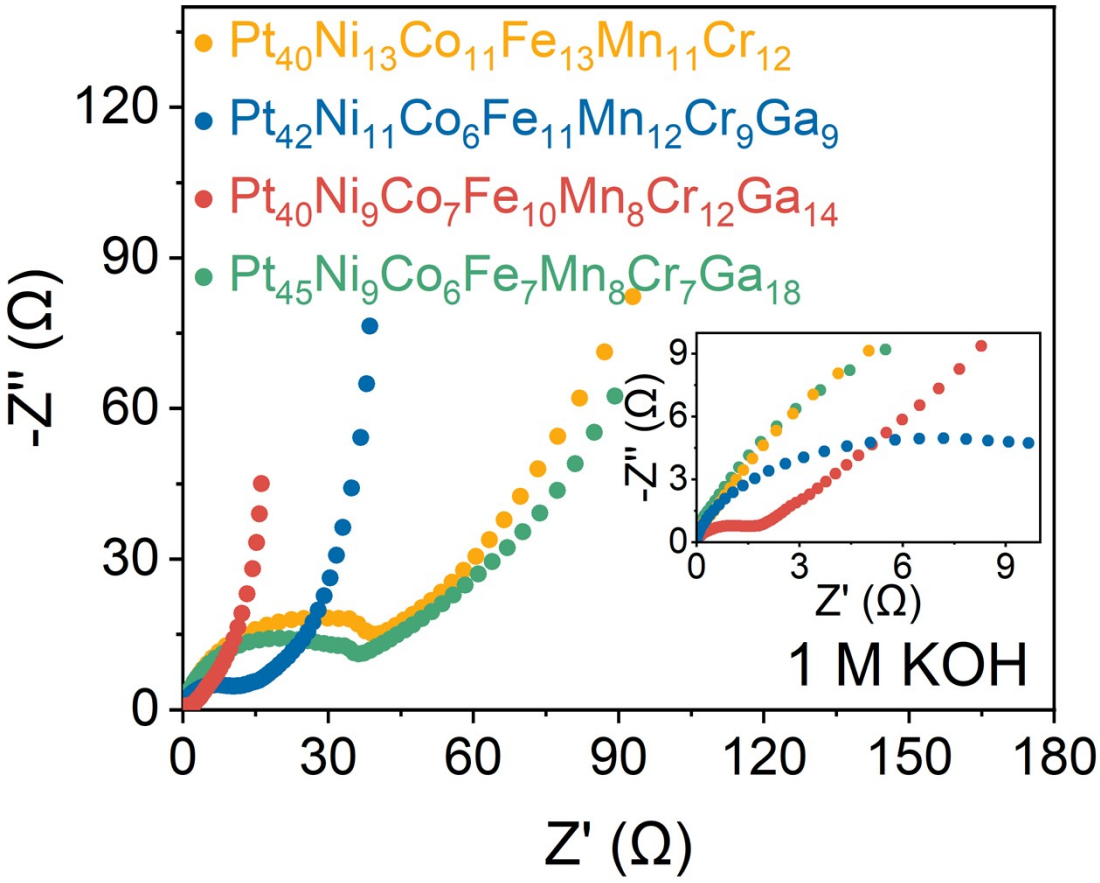

Figure 24. EIS of PtNiCoFeMnCrGa/CNT.

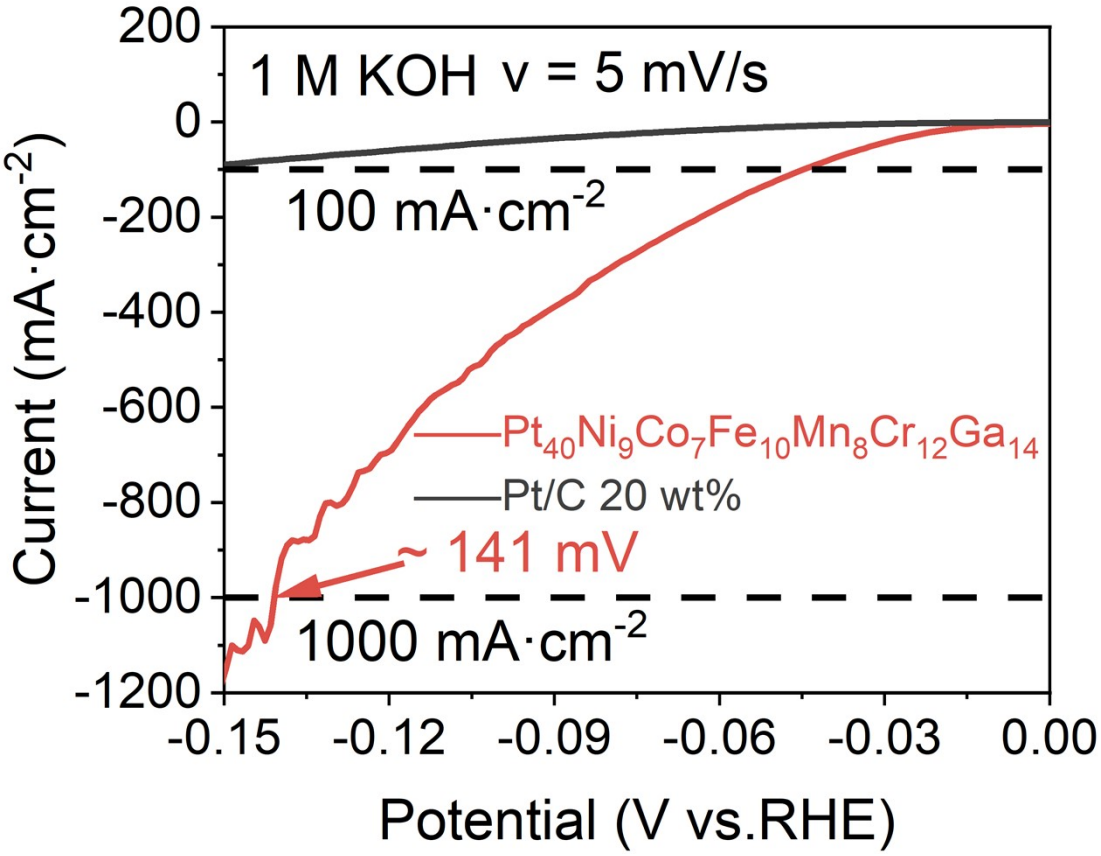

Figure S25. High-current-density LSV of HER of

$Pt_{40}Ni_9Co_7Fe_{10}Mn_8Cr_{12}Ga_{14}$/CNT.

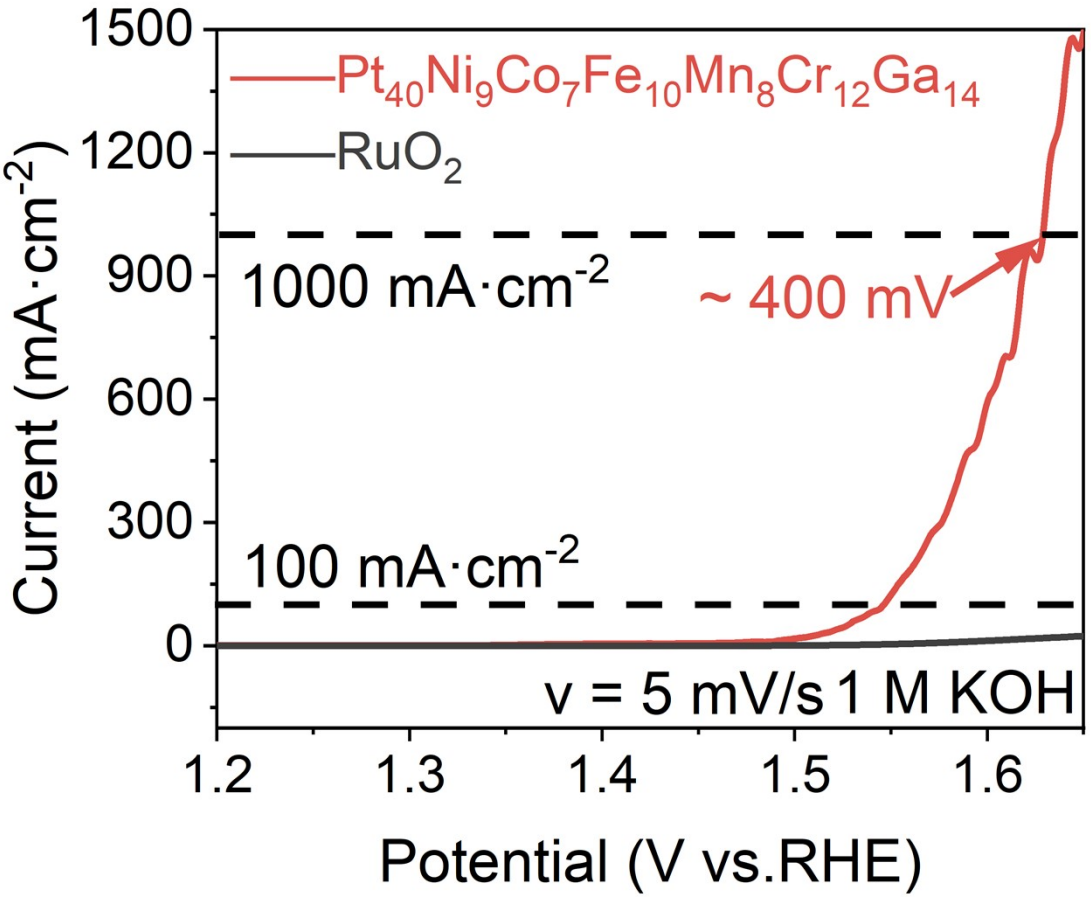

Figure S26. High-current-density LSV of OER of $Pt_{40}Ni_9Co_7Fe_{10}Mn_8Cr_{12}Ga_{14}$/CNT and RuO_2 in 1 M KOH.

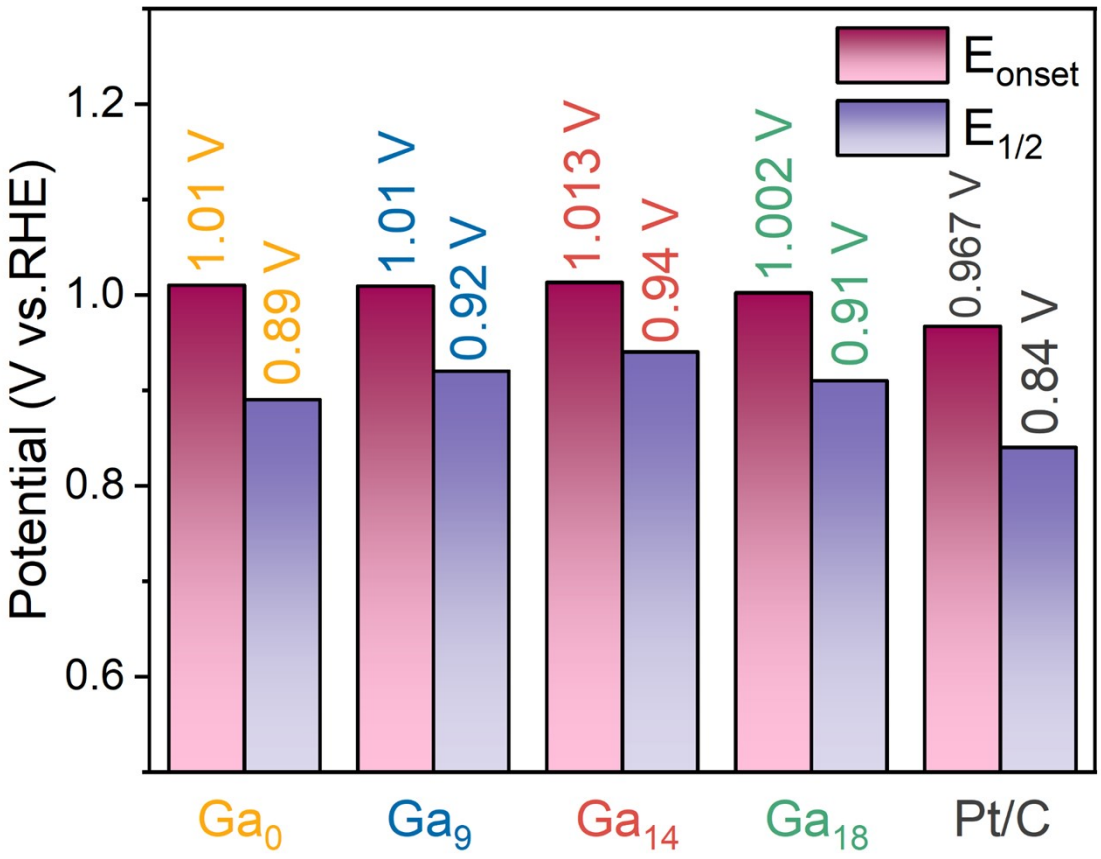

Figure S27. Bar chart of E_{onset} and $E_{1/2}$ in 0.1 M KOH of PtNiCoFeMnCrGa/CNT and Pt/C.

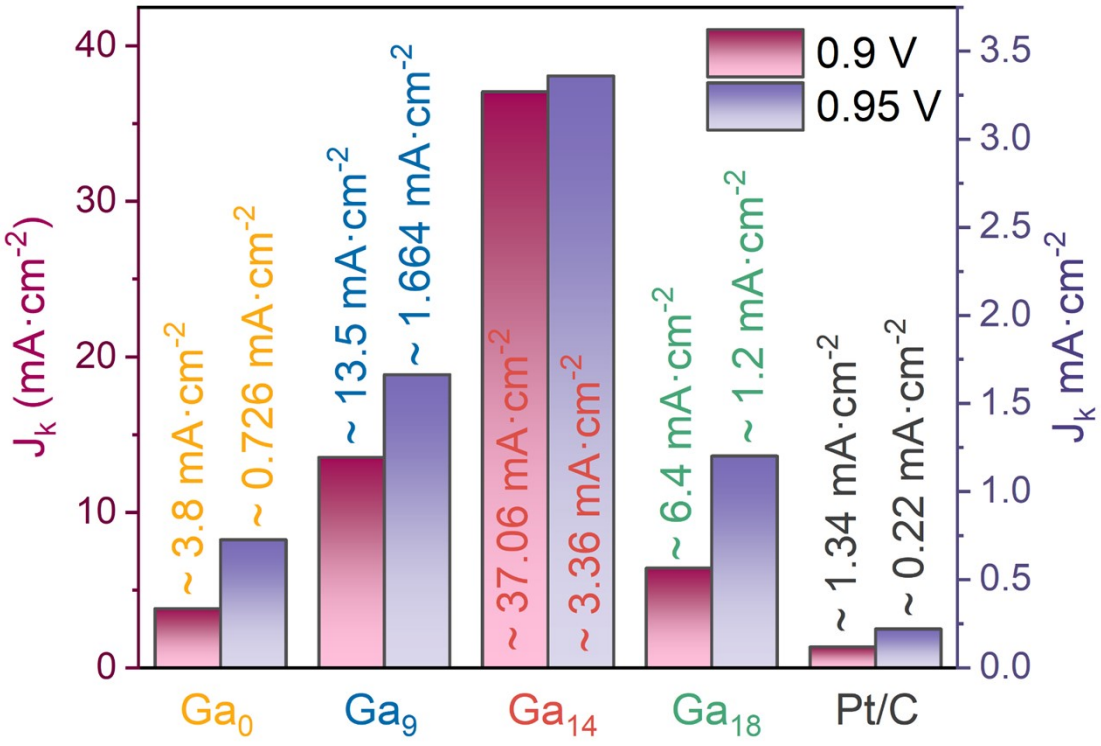

Figure S28. Bar chart of ORR J_k in 0.1 M KOH of PtNiCoFeMnCrGa/CNT and Pt/C.

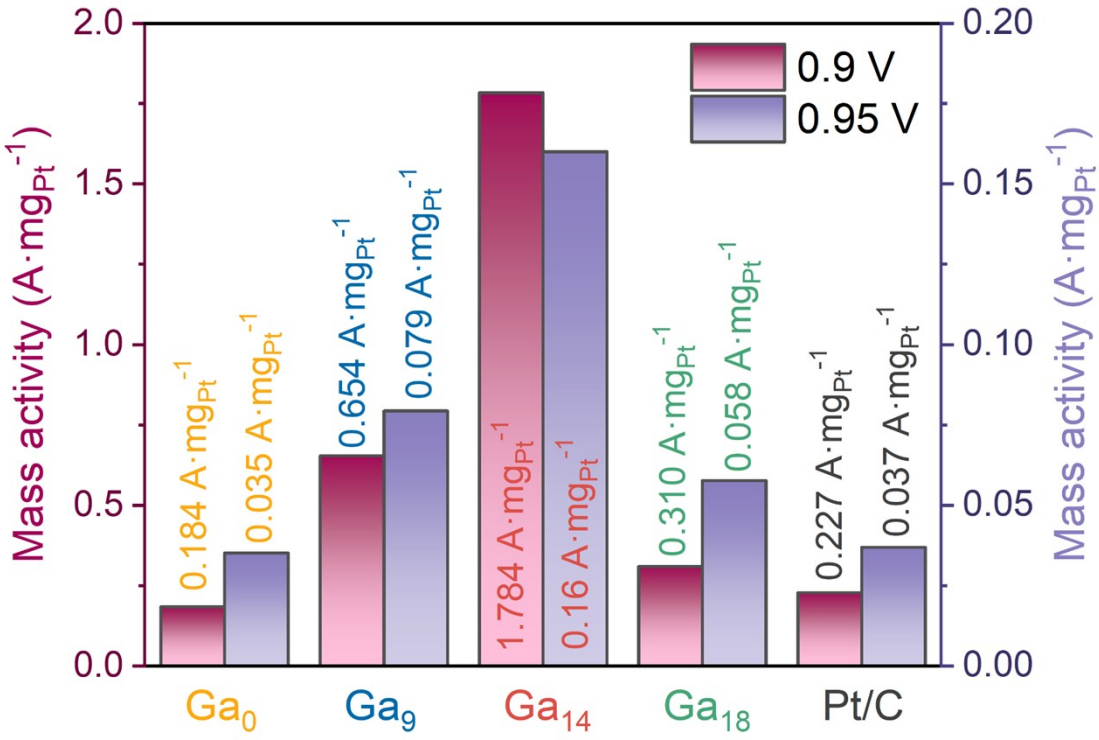

Figure S29. Bar chart of ORR mass activity in 0.1 M KOH of PtNiCoFeMnCrGa/CNT and Pt/C.

Table S1. HER performance for the reported electrocatalysts

Name	Overpotential (mV)	Tafel slop (mV dec^{-1})	Reference
Pt-CuW	41	43.7	[5]
aPt/RuO_2NR/C	18	30.8	[6]
$Pt_{80}B_{20}$/C	37	38.8	[7]
Pt@TGNP	32	28.44	[8]
Pt/$Ni(OH)_2$/NF	42	44.4	[9]
Ni-NiO-Pt	23.54	44.48	[10]
Pt-MoC_x@C	19	30	[11]
Pt/Rh_2O_3-CN_x	26.7	35	[12]
Pt-AC/Cr-N-C	19	30	[13]
$Pt_{78}La_{22}$/C	22	28.15	[14]
Pt-Ni@Re/C NPC	36	30	[15]
O_v-rich H-TiO_2/Pt	35	41.1	[16]

Table S2. OER and ORR performance for the reported electrocatalysts

Name	OER η_{10} (mV)	ORR $E_{1/2}$ (V)	Reference
Co-Pt@Fe-N-C	410	0.89	[17]
PFCN@NT300	397	0.798	[18]
HEA@Pt	370	0.85	[19]
N/Pt/HEA NPs-C	376	0.894	[20]
PtPdFeCoNi/HOPNC	310	0.868	[21]
PtNiCo/P-CA	305	0.92	[22]
ZnFeNiCoCr HEA	305	0.864	[23]
CoCuFeAgRu HEA	280	0.84	[24]
$Fe_2P@FeN_3P_1$-NC	300	0.88	[25]
$Fe_{12}Ni_{23}Cr_{10}Co_{30}Mn_{25}$/CNT	284	0.81	[26]
FeCo/MoN@NCNTs	370	0.845	[27]
Ce-CMO-18%/MWCNTs	341	0.84	[28]
$CoFeS_2@CoS_2$/CNTs	270	0.871	[29]
Co/Ru SAs-N-C	338	0.855	[30]
Sp-Co_3O_4/C EC	380	0.75	[31]

Reference

1. S. Q. Niu, S. W. Li, Y. C. Du, X. J. Han and P. Xu, *ACS Energy Lett.*, 2020, **5**, 1083-1087.
2. Y. Wang, W. Luo, S. Gong, L. Luo, Y. Li, Y. Zhao and Z. Li, *Adv Mater*, 2023, **35**, e2302499.
3. X. Cao, Y. Gao, Z. Wang, H. Zeng, Y. Song, S. Tang, L. Luo and S. Gong, *ACS Appl Mater Interfaces*, 2023, **15**, 32365-32375.
4. L. Ou and S. Chen, *Science China Chemistry*, 2015, **58**, 586-592.
5. L. Chen, X. Jian, P. Zhang, H.-B. Ke and H.-J. Lin, *Journal of Alloys and Compounds*, 2025, **1011**, 178445.
6. J. F. Huang, W. J. Hsieh and J. L. Chen, *ACS Appl Mater Interfaces*, 2024, **16**, 27504-27510.
7. H. Jiang, Y. Xiao, Z. Liu, Z. Wang, B. Wei, Q. Wei and N. Cheng, *J Colloid Interface Sci*, 2025, **684**, 95-104.
8. S. J. Lee, J.-B. Baek and I.-Y. Jeon, *Materials Today Sustainability*, 2024, **28**, 100984.
9. C. Liang, H. Fan, A. Kong, M. Peng, M. Liu, W. Xu, J. Song, Y. Li, J. Zhang, Y. Ding and Z. Conrad Zhang, *Applied Surface Science*, 2023, **629**, 157433.
10. X. Zheng, X. Wu, R. Wan, Y. Wang, B. Chen and G. Meng, *Small*, 2025, **21**, e2411696.
11. L. Chen, Y. Huang, Y. Ding, P. Yu, F. Huang, W. Zhou, L. Wang, Y. Jiang, H. Li, H. Cai, L. Wang, H. Wang, M. Liao, L. Zhao and Z. Fan, *Nano Research*, 2023, **16**, 12186-12195.
12. B. Kumar Manna, R. Samanta, R. Kumar Trivedi, B. Chakraborty and S. Barman, *J Colloid Interface Sci*, 2024, **670**, 258-271.
13. L. Zeng, Z. Zhao, Q. Huang, C. Zhou, W. Chen, K. Wang, M. Li, F. Lin, H. Luo, Y. Gu, L. Li, S. Zhang, F. Lv, G. Lu, M. Luo and S. Guo, *J Am Chem Soc*, 2023, **145**, 21432-21441.
14. Y. Feng, S. Zhang, M. Chen, L. Zhu, A. Pei, F. Wu, X. Liao, Q. Gao, W. Wang, Z. Yang, H. Ye and B. H. Chen, *J Colloid Interface Sci*, 2025, **679**, 918-928.
15. J. Kim, J. Oh, S. Baskaran, T. G. Kim, S. Kim, J. Yang, J. Jung and S. M. Yoon, *Applied Catalysis B: Environment and Energy*, 2024, **347**, 123791.
16. B. Liu, K. Zhang, S. Wei, Y. Zhang, G. Liu, L. Wu and J. Li, *Fuel*, 2024, **376**, 132693.
17. J. Yang, S. Song, Z. Chen, B. Zhang, Y. Guo, Y. Guo and H. Zhang, *Journal of Materials Chemistry A*, 2025, **13**, 6020-6026.
18. T. Braun, S. Dinda, G. Karkera, G. Melinte, T. Diemant, C. Kübel, M. Fichtner and F. Pammer, *ChemistrySelect*, 2023, **8**, 9.
19. P. Zhang, X. Hui, Y. Nie, R. Wang, C. Wang, Z. Zhang and L. Yin, *Small*, 2023, **19**, 2206742.
20. M. Niu, Q. Guan, W. Yuan, C. X. Guo, D. Cao, C. M. Li, L. Y. Zhang and X. S. Zhao, *Chemical Engineering Journal*, 2025, **503**, 158465.
21. M. Xie, Y. Lu, X. Xiao, D. Wu, B. Shao, H. Nian, C. Wu, W. Wang, J. Gu, S. Han, M. Gu and Q. Xu, *Advanced Functional Materials*, 2024, **35**, 2414537.

22. Z. Wang, Z. Wang, J. He, Z. Li, H. Tong, J. Zhang and Z. Chai, *International Journal of Hydrogen Energy*, 2024, **51**, 464-474.
23. J. Li, B. Li, P.-T. Li, N. Zhang and H.-S. Shang, *Rare Metals*, 2024, **44**, 1789-1799.
24. Z. Qiu, X. Guo, S. Cao, M. Du, Q. Wang, Y. Pi and H. Pang, *Angewandte Chemie International Edition*, 2024, **64**, e202415216.
25. E. Zhu, C. Shi, J. Yu, H. Jin, L. Zhou, X. Yang and M. Xu, *Applied Catalysis B: Environment and Energy*, 2024, **347**, 123796.
26. X. Cao, Y. Gao, Z. Wang, H. Zeng, Y. Song, S. Tang, L. Luo and S. Gong, *ACS Appl. Mater. Interfaces*, 2023, **15**, 32365-32375.
27. Y. Zhang, W. Xue, Y. Ding, J. Chen and X. Xu, *Inorganic Chemistry Communications*, 2025, **177**, 114374.
28. X. Chen, F. Han, X. Chen, C. Zhang and W. Gou, *Catalysts*, 2022, **12**, 1122.
29. J. Jeon, K. R. Park, K. M. Kim, D. Ko, H. Han, N. Oh, S. Yeo, C. Ahn and S. Mhin, *Nanomaterials*, 2022, **12**, 983.
30. L. Zhang, J. Yao, J. Zhang, W. He, Y. Li, L. Liang, C. Liu, H. Liu and Q. Hao, *Catalysis Science & Technology*, 2022, **12**, 5435-5441.
31. B. Chutia, R. Chetry, K. N. Rao, N. Singh, P. Sudarsanam and P. Bharali, *ACS Applied Nano Materials*, 2024, **7**, 3620-3630.